Simulation and Model Reduction Methods for an RF Plasma Glow Discharge

Yi-hung Lin and Raymond A. Adomaitis[1]

Department of Chemical Engineering and Institute for Systems Research, University of Maryland, College Park, Maryland 20742

In this paper, we report on numerical solutions and model reduction results for a plasma glow discharge model with a radio frequency ionization source. A pseudospectral implementation of a global spectral method was found to give accurate simulation results that correctly reflected the expected physical behavior of an argon plasma under the simulated operating conditions. Numerical residual analysis was used to confirm solution convergence. Using snapshots taken from the detailed simulations, a reduced basis was generated in terms of two groups of empirically determined eigenfunctions, distinguished by their type of boundary conditions (Dirichlet vs Neumann). With this model reduction approach, it was found that the state variables can be accurately predicted by projecting the original modeling equations onto the reduced basis with considerable computational savings over the original simulations. Limitations of the model reduction method in predicting secondary (derived) quantities are discussed.   © 2001 Academic Press

Key Words: collocation; global basis functions; glow discharge; model reduction; plasma processing; pseudospectral methods.

1. INTRODUCTION

Plasmas with low gas pressure (1 mtorr to 10 torr), temperature (300 to 500 K), and degree of ionization (10^{-6} to 10^{-1}) are used extensively for manufacturing integrated circuits. Plasma processing is a key fabrication step, especially for etching and deposition of thin films. Plasma discharge reactor systems are characterized by a large number of adjustable parameters and poorly understood transport and reaction mechanisms. This has motivated the vigorous development of first-principles models and full-scale simulators in the past decade to study various aspects of plasma processing. However, the numerical solution of the resulting models usually requires substantial computational resources, a primary

---

[1] To whom correspondence should be addressed. Fax: (301) 314-9920. E-mail: adomaiti@isr.umd.edu.

reason being that current simulation techniques inevitably result in a finely resolved spatial discretization mesh in the plasma sheath regions. These large-scale system models are unsuitable for real-time control, efficient simulation, and iterative process optimization. To increase the utility of the existing simulators, model reduction methods must be used to extract the dominant spatial characteristics of the discharge; numerically efficient spectral projection methods are then used to generate the reduced model.

Numerical methods for producing low-dimensional representations of infinite-dimensional systems have been proposed in the context of the theory of approximate inertial manifolds (e.g., the nonlinear Galerkin method [1–4]) and reduced-basis methods such as the proper orthogonal decomposition (POD) [5–7]. Applications include fluid flow simulations in complex geometries [8], rapid thermal chemical vapor deposition [7], rapid thermal processing simulation and control [9, 10], nonlinear model-based process control [2–4, 11], and grooved channel flow reactor control [12–14]. To the authors' knowledge, there have been no similar studies reported on plasma glow discharge processes.

In this study, we report on numerical techniques for computing the radio frequency (RF) discharge solution and demonstrate model reduction results for this system. The model is similar to those used for magnetohydrodynamics simulations and models of this type are commonly used to describe the physics of plasma discharges [15–17]. As the first test of plasma model reduction, the model and boundary conditions are slightly modified from a previous DC simulation [17]: in the current study, the electron diffusivity is assumed to be independent of electron energy and the boundary conditions are made to be homogeneous. A Chebyshev collocation method is used for the spatial discretization of the glow discharge model. The discretized sets of ordinary differential equations are integrated in time using a fully implicit integration method with a Newton–Raphson method solving the nonlinear set of equations at each time step. The detailed simulation data then are used to generate the empirical eigenfunctions using the proper orthogonal decomposition method. Finally, the Galerkin projection method is used with the reduced-basis functions to simulate the dynamics of the reduced model. The performance of the reduced model is compared to the high-degree simulations, and limitations of the reduced-basis discretization methods are also discussed.

2. MODELING EQUATIONS

Complete models of low pressure plasma processing reactors can be conceptually decomposed to three submodels [16, 18] describing: (1) the plasma physics (concentrating on discharge structure); (2) plasma chemistry (also called the reactor model); and (3) surface reactions. The plasma chemistry (neutral transport) models are a natural extension of computational fluid dynamics simulations and are relatively more advanced than the plasma physics model, and the surface reaction model relies on descriptions of the solid state physics of the material undergoing processing; therefore, the plasma physics submodel can be considered the link connecting the three submodels. Once the plasma physics model is complete, the simulator can be coupled with the transport model with an existing computational fluid dynamics (CFD) package such as FLUENT or FIDAP.

A complete model describing the discharge physics will combine the Boltzmann equation with Maxwell's equations. However, all the particle-scale information contained in the Boltzmann distribution function may not be necessary for a particular modeling purpose. An alternative fluid-type approach based on the moments of the distribution may be used

to obtain information on the macroscopic properties of the discharge. These fluid type formulations have had great success in explaining the physics of the glow discharge, and the results can be comparable to those produced by Monte Carlo particle simulation techniques [16]. In this study, the model is equivalent to the modeling equations presented in [17, 19] and the modifications according to [20, 21] are adopted for this RF simulation and model reduction study. The single exception to the cited modifications is that a separate effective electric field meant to compensate for potential errors introduced by applying the diffusion-drift approximation to the ion species balance was not included in this study; under the conditions used for this simulation study, it was found that this effective electric field could be neglected because of the relatively small displacement of ions during an RF cycle. A summary of the major differences between the model used in the current study and the model used in previous simulations by the authors [17] is included below.

1. Electron diffusivity is a constant in both the electron flux and thermal conductivity definitions. The model validity is not significantly affected by this assumption [20, 22] under the operating conditions used in this study. Therefore, the electron and ion fluxes have the same form of diffusion-drift expression.

2. In the electron energy balance equation, the electron density and temperature are combined into the so-called electron energy density; i.e., $n_e(\frac{3}{2}k_b T_e) = n_e \epsilon_e = \omega_e$.

3. The argon ionization coefficient value is based on the experimental data fitted by Richards and co-workers [22].

After nondimensionalization, the following one-dimensional model is used for this RF simulation and model reduction study

$$0 = \frac{\partial E}{\partial z} - \epsilon(u_+ - u_e) \tag{1}$$

$$T\frac{\partial u_e}{\partial \tau} = -\frac{\partial J_e}{\partial z} + ku_e \tag{2}$$

$$T\frac{\partial u_+}{\partial \tau} = -\frac{\partial J_+}{\partial z} + ku_e \tag{3}$$

$$T\frac{\partial \omega}{\partial \tau} = -\frac{\partial Q}{\partial z} - \chi J_e \cdot E - ku_e H_i, \tag{4}$$

where the dimensionless time is defined as $\tau = \nu t$, and the four state variables consist of the voltage Φ, electron number density u_e, ion number density u_+, and electron energy density ω. The dimensionless variables are defined by

$$\Phi = \frac{V}{V_0}, \quad u_e = \frac{n_e}{n_0}, \quad u_+ = \frac{n_+}{n_0}, \quad \text{and} \quad \omega = \frac{T_e n_e}{T_{e0} n_0}.$$

The auxiliary equations for electric field E, electron flux J_e, ion flux J_+, electron energy flux Q, and ionization rate coefficient k are

$$E = -\frac{\partial \Phi}{\partial z}$$

$$J_e = -\frac{\partial u_e}{\partial z} - P_e u_e E$$

$$D_{e+} \cdot J_+ = -\frac{\partial u_+}{\partial z} - P_+ u_+ E$$

$$Q = -\frac{5}{3} \left(\frac{\partial \omega}{\partial z} + P_e \omega E \right)$$

$$k = \begin{cases} D_a(\epsilon_e - 5.3)e^{\frac{-4.9}{\sqrt{\epsilon_e - 5.3}}}, & \text{for } \epsilon_e \geq 5.3 \text{ eV}; \\ 0, & \text{otherwise.} \end{cases}$$

The boundary conditions at $z = 0$ (grounded electrode) are

$$\Phi = 0$$
$$u_e = 0$$
$$\nabla u_+ = 0$$
$$\omega = 0$$

and at $z = 1$ (powered electrode)

$$\Phi = \Phi_{DC} + \Phi_{RF} \sin(2\pi\tau)$$
$$u_e = 0$$
$$\nabla u_+ = 0$$
$$\omega = 0.$$

Source terms accounting for secondary electron emission were not included in the electron number density boundary conditions, in contrast to previous DC simulation studies (e.g., [17]). This simplification is justified because the rate of secondary electron generation is expected to be less than one tenth the ionization rate [20]; a consequence of this simplification is that we should not expect solutions corresponding to a plasma sustained by secondary electrons (the γ discharge, such as shown in [23]). Zero electron density at the boundaries result in the Dirichlet boundary conditions for energy density.

The values and definitions of dimensionless parameters are given in Table I. The gas properties and scaling parameters are listed in Table II. The operating condition and system configuration are selected so that computed results can be compared with previously published simulation results [23–26].

TABLE I
Dimensionless Parameter Values and Definitions
for RF Simulation

Symbol	Definition	Value	Symbol	Definition	Value
ϵ	$\frac{en_0 L^2}{\epsilon_0 V_0}$	723.8	D_{e+}	$\frac{D_e}{D_+}$	3×10^4
D_a	$\frac{k_{io} L^2 N}{D_e}$	955.9	χ	$\frac{eV_0}{\frac{3}{2} k_b T_{e0}}$	100
P_e	$\frac{\mu_e V_0}{D_e}$	25	H_i	$\frac{H_{ei}}{\frac{3}{2} k_b T_{e0}}$	15.578
P_+	$\frac{\mu_+ V_0}{D_+}$	3500	T	$\frac{\nu L^2}{D_e}$	45.2

TABLE II
Gas Physical Properties and Glow Discharge System
Physical Dimensions for RF Simulation

Symbol	Description	Value
L	interelectrode spacing	2 cm
n_0	charge particle reference density	1×10^{10} cm^{-3}
V_0	reference voltage	100 V
$\frac{3}{2}k_b T_{e0}$	reference electron temperature	1 eV
D_+	ion diffusivity	$40 \frac{\text{cm}^2}{\text{s}}$
μ_e	electron mobility	$3 \times 10^5 \frac{\text{cm}^2}{V \cdot s}$
μ_+	ion mobility	$1.4 \times 10^3 \frac{\text{cm}^2}{V \cdot s}$
H_{ei}	ionization enthalpy loss	15.578 eV
V_{DC}	direct current bias	0 V
V_{RF}	RF forcing amplitude	40 V
ν	RF forcing frequency	13.56 MHz
k_{io}	ionization rate prefactor	$8.7 \times 10^{-9} \frac{\text{cm}^3}{\text{s} \cdot \text{eV}}$

3. NUMERICAL METHODS

Current plasma equipment simulators are capable of performing two-dimensional simulations for their specific design purpose; for example, inductively coupled plasma, electron cyclotron resonance reactor, reactive ion etch, or PECVD systems have been simulated individually [27]. The simulators take a first-principles approach by solving the full fluid equations with finite element methods [28] or finite difference methods [29], or by solving the Boltzmann equations with Monte Carlo methods [30, 31], to obtain the spatiotemporal distributions of the state variables. Hybrid methods using both FEM and Monte Carlo methods also have been demonstrated [32, 33]. In this paper, we present the global basis function approach as an alternative to localized basis function discretizations such as finite elements [15] and the block implicit implementation of finite differences [34]. Our approach is motivated by the excellent convergence property of spectral methods [36], their transparency of implementation to discretizing partial differential equations and their boundary conditions, and the great flexibility of selecting and optimizing trial functions for particular applications, e.g., reduced-basis discretization methods. Finally, direct comparisons of the computational cost and numerical accuracy of the reduced-basis and original simulations are simplified when global basis functions are used in all simulations.

In this spectral formulation, the modeling equations and boundary conditions are discretized and solved by a weighted residual method that combines elements of collocation and pseudospectral methods. If each of the states (Φ, u_e, u_+, and ω) is represented by a linear combination of orthogonal trial functions $\psi_i(z)$ defined over $0 \leq z \leq 1$, e.g.,

$$u_e(t, z) = \sum_{i=1}^{N} c_i(t) \psi_i(z), \tag{5}$$

the vector field describing the time evolution of the glow discharge is determined by substituting the trial function expansions into the modeling equations and projecting this residual onto each trial function, subject to the problem boundary and initial conditions. In particular,

the $\psi_i(z)$ are defined in terms of the Lagrange interpolation polynomials for the Chebyshev collocation method [35] used in the detailed simulations of this study. For the reduced-basis simulations, the $\psi_i(z)$ are obtained using the proper orthogonal decomposition technique and the semidiscretized reduced model is produced using the Galerkin projection method [36]. The projection operation is carried out by numerical quadrature on a collocation grid defined by the extrema of a Chebyshev polynomial.

3.1. *Chebyshev Collocation Method and Residual Analysis*

The building blocks of a Lagrange interpolation polynomial are selected as the trial functions ψ_i of (5) for the discrete-ordinate pseudospectral formulation of semidiscretization method used to produce the initial, detailed RF simulation results. The state variables u are approximated using a linear combination of N polynomials of degree $N - 1$; i.e., $u = \sum_{i=1}^{N} c_i(t)\psi_i(z)$, where the building blocks are

$$\psi_i(z) = \prod_{\substack{j=1 \\ j \neq i}}^{N} \frac{z - z_j}{z_i - z_j}.$$

The coefficient c_i represents the value of that state at the discretization point z_i because $\psi_i(z_j) = \delta_{i,j}$ by definition. Because the ψ_i are continuous and differentiable over the entire domain, explicit formulas for differentiation of up to order $(N - 1)$ can be obtained for all z [37]. Once the discretization grid is specified, differentiation becomes a matrix multiplication operation, i.e.,

$$\frac{d\mathbf{u}}{dz} = \mathbf{Ac} \quad \text{and} \quad \frac{d^2\mathbf{u}}{dz^2} = \mathbf{Bc},$$

where the elements of a_{ji} and b_{ji} for the differentiation matrices $\mathbf{A}$ and $\mathbf{B}$ are

$$a_{ij} = \frac{d\psi_j(z_i)}{dz} \quad \text{and} \quad b_{ij} = \frac{d^2\psi_j(z_i)}{dz^2}, \quad i, j = 1, 2, \ldots, N \tag{6}$$

and $\mathbf{c} = [c_1, c_2, \ldots, c_N]^T = [u(z_1), u(z_2), \ldots, u(z_N)]^T$.

In principle, any discretization grid can be used to construct the Lagrange interpolation polynomial. However, the interpolated solutions between discretization points are accurate only if the individual building blocks behave well between the points. Lagrange polynomials constructed with uniformly spaced discretization points will pass through all construction points exactly but will oscillate between points with increasing amplitude near the interval end points ($z = 0, 1$). It has been shown [35] that spacing the discretization points according to a quadratic weight function will suppress the spurious oscillations near the interval end points. In this study, the discretization positions are chosen as the Chebyshev extrema distribution,

$$z_j = \frac{1}{2}\left(\cos\left(\frac{(j-1)\pi}{N-1}\right) + 1\right), \quad j = N, N - 1, \ldots, 1. \tag{7}$$

In the limit of the endpoints, the Chebyshev node spacing is inversely proportional to the square of the total number of points used. This suggests that these polynomial trial functions

can resolve features with length scales of order N^{-2} in the sheath regions while retaining good convergence properties in the bulk phase (see the discussions in [36, p. 40].

Having defined the discretization points and the discrete differentiation operators, the four modeling equations are discretized to give $3(N-2)$ ordinary differentiation equations (ODEs) in time and $(N-2)$ linear algebraic equations (from the Poisson equation) plus eight linear equations from the boundary conditions. The set of discretized system of equations is integrated in time using the fully implicit backward-Euler algorithm using the Newton–Raphson method to solve the nonlinear equations at each time step. The modeling equations describing the time-integration method can be written as

$$\mathbf{AE}^{k+1} - \epsilon \left(\mathbf{u}_+^{k+1} - \mathbf{u}_e^{k+1} \right) = \mathbf{0}$$

$$\mathbf{u}^{k+1} + \frac{\Delta t}{T}(\mathbf{A\Gamma}^{k+1} - \mathbf{G}^{k+1}) = \mathbf{u}^k$$

(8)

$$\mathbf{Lu}^{k+1} = c,$$

(9)

where Δt is the given time step size while k denotes the current step; the first equation is the discretized Poisson equation (1); $\mathbf{u}$, $\mathbf{\Gamma}$, and $\mathbf{G}$ represent discretized values of u_e, J_e, and ku_e (respectively) in the electron continuity equation (2), or u_+, J_+, and ku_e for the ion continuity equation (3), or ω, Q, and $(\chi J_e \cdot E + ku_e H_i)$ for electron energy density equation (4). Equation (9) represents the eight boundary conditions; the linear operator $\mathbf{L}$ is the discretized first-order differentiation array $\mathbf{A}$ when (9) represents the ion boundary condition, or is the identity array otherwise. The c in (9) is zero except when (9) corresponds to $\mathbf{\Phi}(z = 1)$, for which it is $\mathbf{\Phi}_{RF} \sin(2\pi\tau)$.

There are two advantages of using the fully implicit backward Euler algorithm. First, it is simple to implement and is unconditionally stable. The second advantage is that the time increment can be fixed so that at each time step the only computation is the Newton–Raphson iteration. By storing the solution calculated over the entire previous RF cycle and using these as the corresponding initial guesses for the Newton–Raphson procedure for points during the next cycle, the number of iterations required to reach converged solutions is significantly decreased. An additional advantage will be discussed in the following section.

The convergence of the computed solutions (in terms of trial function truncation number N) can be assessed by examining the weighted 2-norm of the time derivative or residual functions (right-hand sides of Eqs. (1)–(4)) plotted as a function of the spatial discretization level (N) of the modeling equation. In this study, a two-level grid method was implemented to numerically conduct this residual analysis for the collocation solution. The time derivative/residual function is obtained by substituting the solution, interpolated to a sufficiently fine grid (sufficiently fine to provide a converged approximation to the residual function), into the modeling equations. Neville's algorithm [38] is used for this high degree interpolation. This interpolation algorithm is based on rearranging the Lagrange interpolating polynomial and noting that any interpolated value of the polynomial, passing through $z_i, z_{i+1}, \ldots, z_{i+m}$, can be obtained by the values of two lower degree polynomials, passing through z_i to z_{i+m-1} and z_{i+1} to z_{i+m}. A tableau of values thus is established from the zeroth degree polynomials, passing through only one point, to the highest degree, which is the interpolated result.

This residual analysis requires the definition of quadrature operations on the finer-scale discretization grid. The quadrature weights associated with the Chebyshev extrema are

obtained by noting that choosing this node distribution implicitly implements the Chebyshev polynomial expansion, which can be evaluated with the exact formula

$$T_n(z) = \cos(n \cos^{-1}(z)), \quad n = 0, 1, 2, \ldots.$$

Thus, the quadrature weight array $\mathbf{w}$ associated with the Chebyshev extrema grid $\mathbf{z}$ can be obtained by

$$\mathbf{w} = (\bar{\mathbf{Q}}\mathbf{Q}^{-1})^T \bar{\mathbf{w}}, \tag{10}$$

where $Q_{i,j} = T_{j-1}(z_i)$ and $\bar{Q}_{i,j} = T_{j-1}(\bar{z}_i)$ for $i, j = 1, 2, \ldots, N$. Therefore, $\bar{\mathbf{Q}}$ is the Chebyshev polynomial interpolation array evaluated on the Gauss–Lobatto quadrature grid $\bar{\mathbf{z}}$ computed using the software described in [39].

3.2. *Limit-Cycle Fixed-Point Methods*

Defining $\mathbf{v}$ as the vector of the spatially discretized state variables $\mathbf{\Phi}, \mathbf{u_e}, \mathbf{u_+}$, and $\boldsymbol{\omega}$, we can write the time-discretized set of equations that result from the backward-Euler integration method (8, 9) as

$$\mathbf{g}(\mathbf{v}^{k+1}, \mathbf{v}^k) = \mathbf{0}.$$

The limit-cycle fixed-point algorithm is based on finding the limit-cycle initial condition $\mathbf{v}^1$ such that

$$\mathbf{v}^{ns} - \mathbf{v}^1 = \mathbf{0}, \tag{11}$$

where $ns - 1$ is the number of time intervals used in the backward-Euler integration method per RF cycle. Using a subscript to denote fixed-point algorithm iteration number, linearizing (11) at the initial condition $\mathbf{v}_i^1$ gives

$$\mathbf{0} = \mathbf{v}_i^{ns} - \mathbf{v}_i^1 + \left(\frac{\partial \mathbf{v}_i^{ns}}{\partial \mathbf{v}^1} - \mathbf{I} \right) \left(\mathbf{v}_{i+1}^1 - \mathbf{v}_i^1 \right),$$

which is solved for the initial condition update $(\mathbf{v}_{i+1}^1 - \mathbf{v}_i^1)$.

To compute the derivatives $\partial \mathbf{v}_i^{ns}/\mathbf{v}^1$, $\mathbf{g}$ is linearized at a solution $(\mathbf{v}^{k+1}, \mathbf{v}^k)$ to $\mathbf{g} = \mathbf{0}$ and the following arrays are defined

$$\mathbf{J}^{k+1} = \frac{\partial \mathbf{g}}{\partial \mathbf{v}^{k+1}} \quad \text{and} \quad \mathbf{C} = \frac{\partial \mathbf{g}}{\partial \mathbf{v}^k}.$$

We find

$$\frac{\partial \mathbf{v}^{k+1}}{\partial \mathbf{v}^k} = -[\mathbf{J}^{k+1}]^{-1}\mathbf{C}$$

and

$$\frac{\partial \mathbf{v}^{k+n}}{\partial \mathbf{v}^k} = (-1)^n [\mathbf{J}^{k+n}]^{-1}\mathbf{C}[\mathbf{J}^{k+n-1}]^{-1}\mathbf{C}\ldots[\mathbf{J}^{k+1}]^{-1}\mathbf{C}.$$

The overall procedure for computing the updated set of initial state variable profiles comes at little additional computational cost because $\mathbf{J}$ is the Jacobian array associated with solving (8, 9) and $\mathbf{C}$ is a constant array consisting of (-1) on the diagonal elements corresponding to each semidiscretized ordinary differential equation in time (and zeros elsewhere).

3.3. *POD–Galerkin Method*

The large number of discretization points required to resolve the sheath regions and the many RF cycles required to asymptotically approach an equilibrium solution make RF solutions computationally expensive. This motivates the development of the reduced-basis projection method used in this study to obtain a reduced-order model.

In the overall POD–Galerkin projection approach to producing reduced-order models, each state variable is defined by a global trial function expansion (as in Eq. (5)), where the trial functions ψ_i are replaced by those ϕ_i obtained by the proper orthogonal decomposition method, a technique for generating an optimal basis for time-varying state variables [8]. Consider the ensemble $\{u^k\}$ of scalar fields, each being a function $u = u(z)$ defined on the domain [0, 1]. The goal is to find a basis $\{\phi_j(z)\}_{j=1}^{\infty}$ for a subspace of a Hilbert space $L^2([0, 1])$ that is optimal for the data set $\{u^k\}$ in the sense that truncated sequences of the form

$$u_N(z) = \sum_{j=1}^{N} a_j \phi_j(z)$$

describe a typical member of the ensemble better than representations of the same truncation number N in any other basis. The resulting mathematical statement of optimality can be reduced to an eigenvalue problem [5]

$$\int_0^1 \langle u(z)u^*(z')\rangle \phi(z')\, dz' = \lambda \phi(z), \tag{12}$$

where the $*$ denotes the complex conjugate. The eigenfunctions ϕ_i of this two-point spatial correlation operator form a set of orthogonal functions satisfying the same homogeneous boundary conditions as the u^k while the eigenvalues λ_i quantify the probability of the occurrence of the ϕ_i in the ensemble. Because

$$\lambda_i = \langle (u, \phi_i)^2 \rangle,$$

where $(\cdot, \cdot)$ and $\langle \cdot \rangle$ denote the inner product and the ensemble average, respectively, the mean square error due to the truncation is

$$\bar{\varepsilon}^2 = \sum_{j=N+1}^{\infty} \lambda_j.$$

In other words, the "energy" captured can be quantified by the sum of the eigenvalues corresponding to the modes used in the solution expansion $u_N(z)$.

Direct solution methods for the eigenvalue problem (12) can become computationally prohibitive when the function u is represented by a high degree, trial function expansion, such as in highly resolved finite element simulations. To overcome this numerical limitation, the basis functions ϕ_i may be found by the method of snapshots or strobes [40]. Suppose that $\{u^i\}_{i=1}^{M}$ are spatially discretized snapshots of the state variable field u and that the weighted inner product on the N-dimensional vector space is denoted by $(\cdot, \cdot)$, that is, the discretized version of the inner product in $L^2([0, 1])$. If ϕ is an eigenvector then

$$\phi = \sum_{k=1}^{M} b_k u^k,$$

where the coefficients b_k remain to be determined. The N-dimensional eigenvalue problem analogous to (12) may then be written as

$$\left(\frac{1}{M}\sum_{i=1}^{M}u^i \otimes u^i, \sum_{k=1}^{M}b_k u^k\right) = \lambda\sum_{k=1}^{M}b_k u^k, \tag{13}$$

where $\otimes$ is the tensor product. The left-hand side of (13) can be rearranged to give

$$\sum_{i=1}^{M}\left[\sum_{k=1}^{M}\frac{1}{M}(u^i, u^k)b_k\right]u^i(x),$$

and the sufficient condition for the solution of (13) will be to find coefficients b_k such that

$$\sum_{k=1}^{M}\frac{1}{M}(u^i, u^k)b_k = \lambda b_i; \quad i = 1, \ldots, M. \tag{14}$$

This is now an $M \times M$ eigenvalue problem to be solved for the snapshot linear combinations **b** that define the discretized reduced-basis functions. This problem is readily solved using the singular value decomposition function in MATLAB; the **b** correspond to the left singular vectors of the array of snapshot inner products, and the eigenvalues correspond to the singular values of the same. Finally, we note that the snapshots $\{u^i\}_{i=1}^{M}$ must be linearly independent to generate M orthogonal eigenfunctions defined by the vectors **b**, and that the POD method does not give a criterion in choosing M; therefore, numerical tests must be conducted to determine when a sufficiently "converged" basis is found.

3.3.1. Galerkin projection numerical methods. Having computed one or more reduced-bases with the POD method, the reduced model is produced by projecting the original, nonlinear modeling Eqs. (1)–(4) onto these spatially discretized trial functions (note that a variable transformation for $\mathbf{\Phi}$ is used to make the boundary condition at $z = 1$ homogeneous). The trial functions are discretized on a Chebyshev extrema grid (7) and the same discrete differentiation arrays are used as in Eq. (6) as part of the numerical, semidiscrete Galerkin projection. The quadrature weights required in the Galerkin projection are obtained using Eq. (10).

With the empirical eigenfunctions satisfying all boundary conditions, the four modeling equations are discretized to give $(2N_1 + N_2)$ ODEs in time and N_1 linear algebraic equations (resulting from the Poisson equation), where N_1 is the number of trial functions used to approximate $\mathbf{\Phi}$, u_e, and ω, while N_2 is the truncation number for u_+ expansion (the difference between N_1 and N_2 is a result of the different types of boundary conditions). The same implicit time integration method used previously in the Chebyshev collocation simulations is employed again. The set of equations for the time integration of u_e, u_+ and ω can be written as

$$\mathbf{u}^{k+1} + \frac{\Delta t}{T}\mathbf{P}_i(\mathbf{A}\mathbf{\Gamma}^{k+1} - \mathbf{G}^{k+1}) = \mathbf{u}^k,$$

where the notation is similar to Eq. (8), but **u** now represents the mode amplitude coefficient vectors and $\mathbf{P}_i$ is the discretized projection operator corresponding to eigenfunctions $\mathbf{\Psi}$ of set i. Note that mode amplitude coefficients for the voltage trial function expansion can be defined explicitly as a function of electron and ion number densities through the Poisson

equation; i.e.,

$$\mathbf{a} = \epsilon(\mathbf{P_1}(\mathbf{B}\mathbf{\Psi_1}))^{-1}(-(\mathbf{P_1}\mathbf{\Psi_2})\mathbf{c} + (\mathbf{P_1}\mathbf{\Psi_1})\mathbf{b}),$$

where the mode coefficients $\mathbf{b}$ and $\mathbf{c}$ correspond to the electron number density and ion number density, respectively.

4. COMPUTATIONAL RESULTS AND DISCUSSION

4.1. *Results for a Representative RF Case*

Detailed simulation results for argon RF discharges under various operating conditions have been reported in the literature [15, 16, 23–26]. The purpose of this simulation study is to show that accurate results can be obtained using global spectral methods, and to provide the snapshot data for the POD method as part of the model reduction procedure.

Figure 1 shows a representative solution obtained using 100 discretization points to represent the particle densities, voltage field, and electron temperature over one RF cycle. The interelectrode spacing was set at 2 cm and the operating conditions corresponded to 1 torr gas pressure and 40 volts RF forcing amplitude. The simulation initial conditions consisted of flat particle density profiles; initial ion density was one thousandth of the target mean value and electron density was one tenth of that of the ions. Solutions obtained using different initial values for voltage and electron energy were investigated; these simulations all asymptotically approached the same limit-cycle solution. For the long-term time-integration simulations, the solution was considered to be converged onto a limit cycle when the 2-norm of the difference between the beginning and end of the cycle for the state variables passed below a preselected value of 10^{-8}. Likewise, the Newton–Raphson iterations were stopped when the norm of the difference between initial and final states reached the same value.

Snapshots of the solution profiles corresponding to a limit-cycle solution are shown at four phases of an RF cycle in Fig. 1 (solutions obtained by integrating over 2000 RF cycles are essentially identical to those obtained by the fixed-point algorithm). The solution plots qualitatively agree with many of the reported physical phenomena characteristic of argon plasmas [15, 16]. The ion density profile is essentially constant over the cycle while electrons instantly respond to the voltage modulation. The plasma sheath thickness reaches 0.3 cm near the cathode, and the plasma potential is approximately 20 volts. Voltage distribution is flat in the bulk phase, showing the quasineutral property of the plasma, and is steeply sloped in the sheaths. Thus, as shown in the electric field distribution plot, the major electric driving force is located in the sheath.

Electron energy is also modulated with the electrode voltage variations. The mean energy distribution is flat in the bulk and has maximum magnitude inside the momentary cathode sheath. Because the ionization rate depends on both the electron number density and the electron energy, the ionization peak occurs at the momentary cathode sheath/bulk boundary (compare the energy and the ionization rate plots), where the number of high energy electrons is sufficient to undergo a significant electron-impact ionization reaction.

The plots of electron, ion, displacement, and total currents shown in Fig. 2 (corresponding to the same solution shown in Fig. 1) quantitatively agree with the total current reported in [23] despite the omitted effect of secondary electrons. Because the generation of secondary electrons contributes to sustaining the discharge, the total current needed to maintain the discharge should be lower. Qualitatively, the plot of plasma current profiles also reflects the
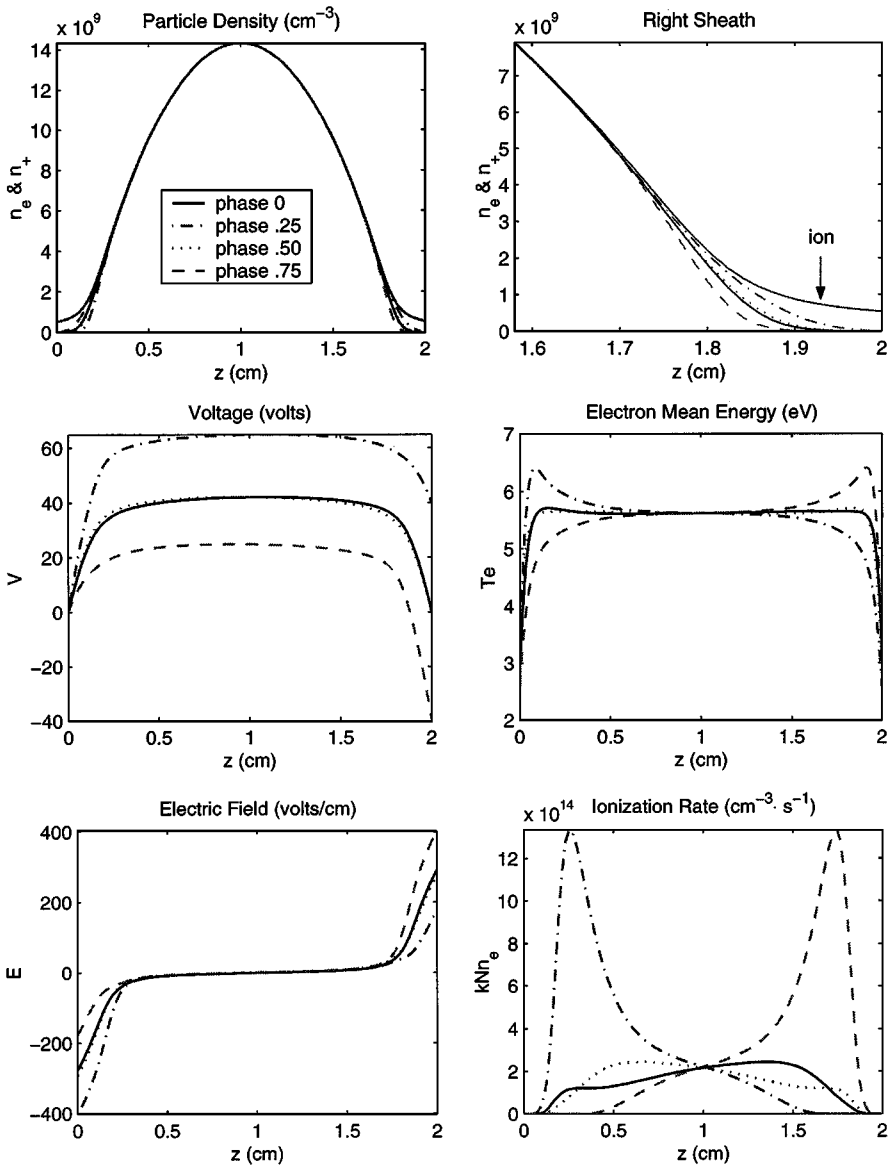
FIG. 1. Argon RF discharge solution corresponding to a converged limit cycle at 1 torr pressure, 2-cm interelectrode spacing, and 293 K. Note that the ion particle density profile remains essentially constant during the RF cycle.

physics of the discharge. Ion currents, modulated inside the sheaths, are almost straight in the bulk phase due to the ambipolar diffusion effect (see Fig. 1). Electrons are the major current carrier in the bulk phase while displacement currents dominate inside the sheaths. The ion current only contributes 10% of the total current. The sum of electron, ion, and displacement currents is a constant due to the current conservation law, which can be derived using the Poisson equation (1), particle continuity equations (2) and (3), and the definition of displacement current (see [41]). The current characteristics reflect the capacitive nature of the argon discharge; i.e., the sheaths behave like capacitors while the bulk phase behaves like a resistor. The regions are connected sequentially as a unit in the entire electrical circuit.
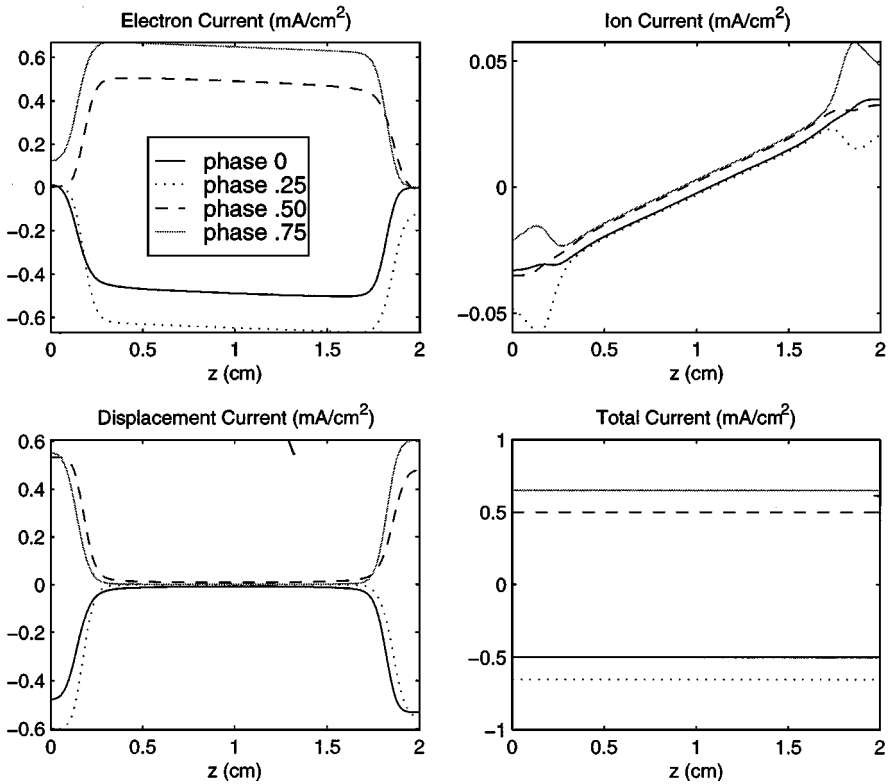
FIG. 2. Snapshots of current profiles in the RF simulation.

Figure 3 shows the ion current (at the powered electrode) and the total current responding to the driving voltage over an RF cycle. The four phases used in Figs. 1 and 2 are also marked on the sine curve of the voltage plot. The ion current and the total current curves are interpolated from the current values at the four phases ($0°$, $45°$, $90°$, and $135°$) using a Fourier series. It is interesting to note that the total current has an approximate $20°$ phase lead with respect to the controlled voltage while the ion current follows the phase of the voltage waveform.

The simulation results demonstrate both the correct physics of the discharge model and the challenges the model presents to the numerical solution techniques. As shown, the primary characteristic of plasma is the thin boundary layers. What distinguishes RF discharge simulations from many computational fluid dynamics computations is that the solution convergence depends on resolving the boundary layers rather than large-scale structures. Independent of what numerical techniques are used, the trial functions must be able to resolve the details of the interphases and the sheaths. Insufficient resolution of these regions will cause problems in terms of solution convergence. The solution shown in Fig. 1 is produced by the Chebyshev collocation method with 100 collocation points. This "coarse" grid solution is interpolated with 250 Gauss–Lobatto points and the interpolated solution is substituted into the modeling equations to obtain the time derivative and residual functions (see Eqs. (1)–(4)). The 2-norms of these functions are plotted in Fig. 4 as a function of the truncation number corresponding to the number of solution collocation points used.

The residual analysis (Fig. 4) confirms that the solution found under this operating condition can be considered a converged solution. Because the Poisson equation is an ordinary
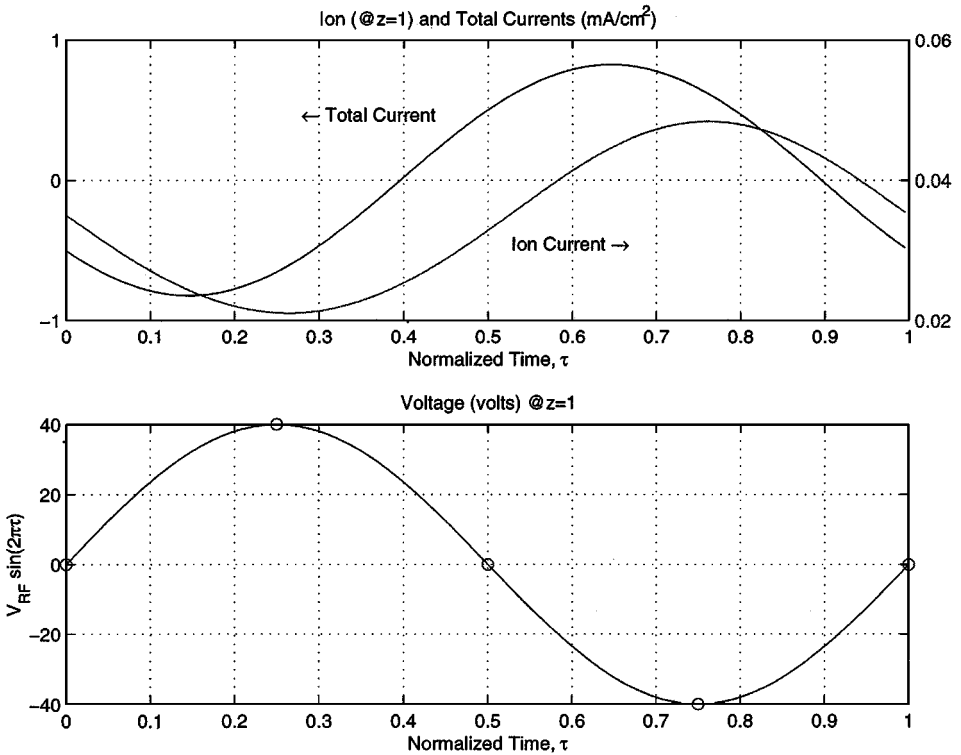
FIG. 3. Ion current at the powered electrode and total current as a function of the applied voltage in the RF simulation.

differential equation, as the number of collocation points N increases, the residual function (Eq. (1)) norm approaches zero. For the other three partial differential modeling equations, the norm of the time derivative functions (see the right-hand side of Eqs. (2)–(4) approaches (RF-cycle average) constants because of the nonzero time derivative functions. The residual plot serves as a good criterion for the measuring trade-off between computational efficiency and solution discretization accuracy.
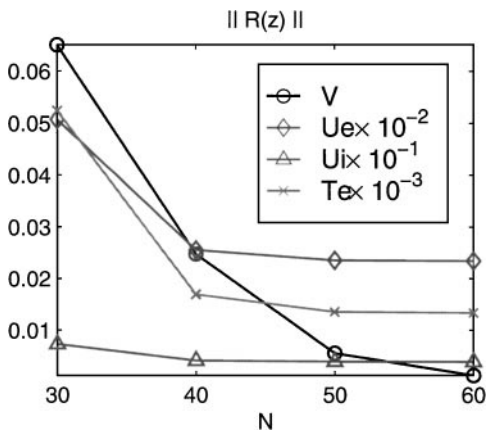

FIG. 4. Residual analysis for RF simulation.

4.2. *RF Simulation Model Reduction*

4.2.1. Optimal discretized basis functions from POD. The computational efficiency of the POD-based model reduction method results from extracting the minimum number of uncorrelated spatial characteristics of the existing solutions and using the principal spatial structures of the solutions to spectrally discretize the original, nonlinear modeling equations. Because each empirical eigenfunction is better tailored to capturing the spatial features of the solution, relatively few trial functions are needed to predict the true system's dynamics. This translates directly into significant computational saving over the simulations based on orthogonal polynomial or other general trial function expansions. As discussed in Section 3.3, the truncation number of the empirical eigenfunction expansions can be conveniently determined using the eigenvalue associated with each POD mode. In this section, the empirical eigenfunctions are generated from the simulation data obtained in previous section, and the performance of the reduced model is demonstrated in the next section.

Figure 5 shows the empirical eigenfunctions and the scaled "solution snapshots" used to generate the reduced basis. The purpose of this model reduction study is to accurately predict with the reduced model the dynamic behavior that includes the start-up transient and the limit-cycle behavior (a goal similar to [8]). Therefore, snapshot data were collected from a transient simulation starting from the stated initial condition to a state near the limit
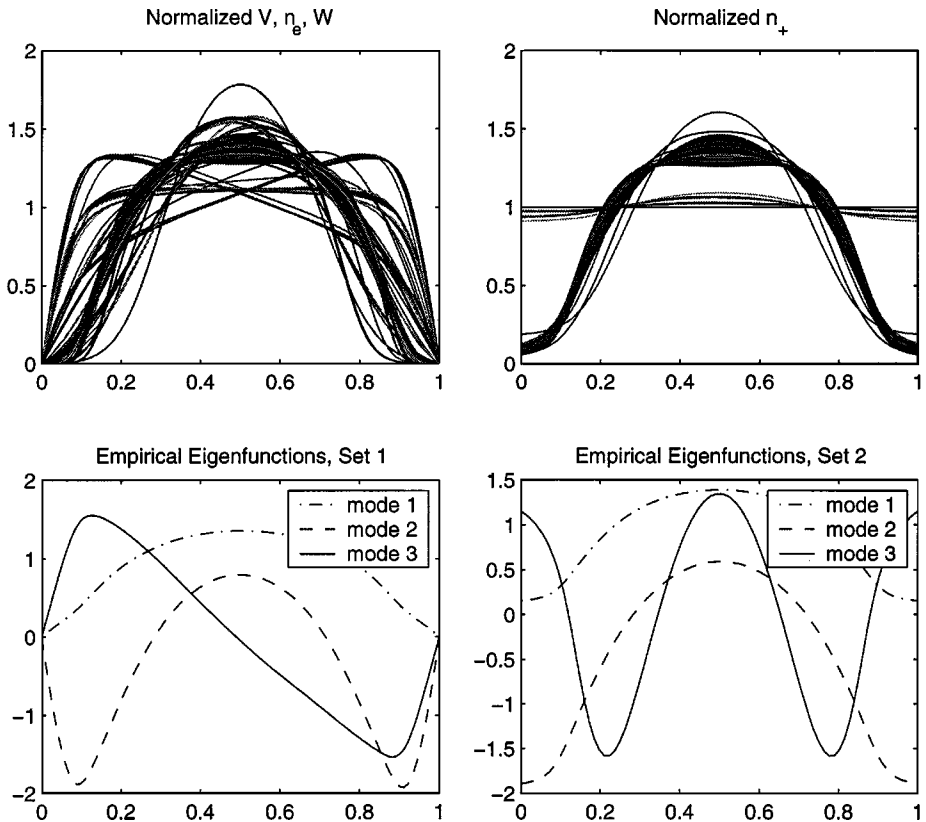
FIG. 5. Snapshots (top) and empirical eigenfunctions (bottom) generated using the proper orthogonal decomposition.

cycle. In this study, a set of approximately 60 snapshots selected from the first 1000 RF cycles were used.

Instead of generating four sets of empirical eigenfunctions, the solution profile snapshot data are classified into two sets according to the form of their boundary conditions. The first set corresponds to the state variables that are subject to Dirichlet boundary conditions; it includes electron density, energy density, and voltage (after the variable transformation is applied making the boundary condition homogeneous at the powered electrode) profile snapshots. The three sets of solution snapshots after scaling are shown in the top left of Fig. 5. Concatenation of the solution snapshots into a single snapshot array for the POD procedure exploits the possible correlations among the three state variables, potentially reducing the total number of empirical eigenfunctions needed for the subsequent projection methods. The second set of functions corresponds to snapshots of ion density profile, which must satisfy vanishing first-derivative boundary conditions.

Sorting the snapshot data according to boundary condition type has an additional beneficial effect on the resulting reduced bases. As discussed earlier, the mass of the (positively) ionized gas species relative to the electrons results in little change of the ion number density profile during an RF cycle, while the other three states (electron density, voltage, and electron energy density) are strongly modulated by the momentary cathode voltage. This gives the ion number density profile a largely symmetric form (with respect to z) compared to the other states. Therefore, adding snapshots of the other fields to the ion density snapshots unnecessarily introduces asymmetry. This property is dramatically shown in the empirical eigenfunctions presented in Fig. 5; compare the highly nonsymmetric third mode of Set 1 to the relatively symmetric third mode of Set 2.

Table III shows the percentage of the accumulated energy (the normalized partial sum of eigenvalues) associated with two sets of empirical eigenfunctions produced by the POD method. Both sets have a dominant first mode, which captures the major characteristics of the solution profiles. The second and higher modes tailor the solution profiles to describe the finer structure. At first glance it appears that using the first three to five modes from each set would be sufficient to produce accurate solutions using the reduced-order model. However, we found that a truncation number $N_2 = 8$ was necessary for the ion density profile expansion while $N_1 = 22$ was used for the remaining state variable trial function expansion truncation numbers. Analysis of this discrepancy is provided in Section 4.2.4.

4.2.2. Reduced-model simulation results. The reduced-order model is produced by semidiscretizing the original RF plasma modeling equations using the Galerkin projection

TABLE III
Accumulated Energy Captured by the
Empirical Eigenfunctions

Set 1			Set 2		
Mode	λ_i	%	Mode	λ_i	%
1	181.86	96.22%	1	61.7113	97.9544%
2	5.39	99.08%	2	1.1927	99.8475%
3	1.34	99.78%	3	0.0897	99.9898%
4	0.34	99.96%	4	0.0062	99.9996%
5	0.03	99.98%	5	0.0001	99.9998%

method and the empirical eigenfunctions shown in the Fig. 5. Each state variable is represented in terms of a linear combination of the empirical eigenfunctions that satisfy the appropriate boundary conditions. An important difference from the previously described collocation method is each computational step in time involves projections by quadrature. It was found that 60-point Chebyshev extrema quadrature integration of these eigenfunctions essentially produce converged inner product computations and that little accuracy was gained using finer discretization grids for the reduced-model simulations (cf. the 100 points used to obtained the snapshot data).

Figure 6 (left column) shows representative results produced by the reduced-order model corresponding to the 250th and 500th RF cycle (computed by integrating the reduced model
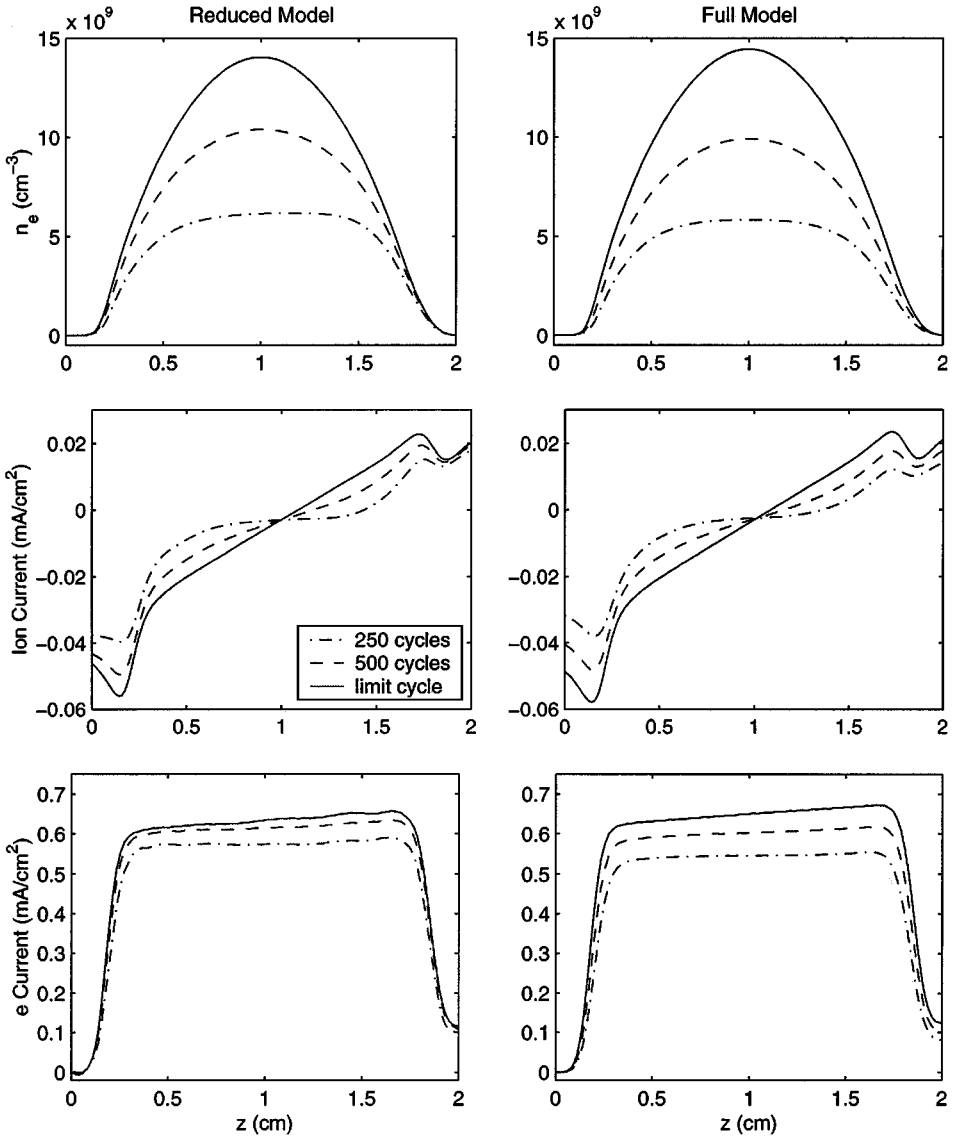
FIG. 6. Performance of the reduced model. The left column shows the solutions during the 250th, 500th, and limit RF cycle for the reduced model while the right column corresponds to the original solution snapshots at the same points in time.

over each time interval) and a point on the limit-cycle solution (computed using the fixed-point algorithm). The initial condition for the limit cycle procedure was chosen as the profiles corresponding to the start of the 250th cycle; we note that at that point in the simulation, the values of $u_e(z)$ and $u_+(z)$ are less than half their steady-state values. This gives some indication of the excellent convergence properties of the fixed-point algorithm. The right column shows the full-order simulation results at the same points in time for comparison. The reduced-order model predictions of the state variable profiles are accurate with only minor errors visible for electron density inside the sheaths. The ion density and currents, which are of primary importance in plasma processing applications, are particularly accurate when compared to the detailed simulations. We note that these profiles were not used in the original snapshot data for generating the empirical eigenfunctions. Minor differences between the full and reduced-order simulator predictions can be seen in the electron current profiles—these differences will be discussed in Section 4.2.4.

4.2.3. Comparison of computational costs. A summary of the computational costs of the full and reduced-order simulations are presented in Table IV. In this table we present a comparison of the execution time and floating point operation counts of the simulations, the limit-cycle fixed point solution procedures, and the computational effort required to implement the POD procedure. We also include results for both the reduced and full-order models for different total simulation RF cycles to demonstrate how using values from previous converged cycles improves the efficiency of the implicit-Euler time integration method. Typically, we find that roughly 80% of the computational cost can be attributed to the semidiscretized function evaluations used to compute the Jacobian array elements by centered finite differences in the full model; this percentage rises to 90% for the reduced model, where the remaining operations, such as computing the update vector for the Newton–Raphson iterations in the implicit-Euler integrator, become proportionally less important. All computations were performed using compiled MATLAB functions on a Sun Microsystems Ultra 10 workstation. Overall, the computational costs of the reduced-model simulations were found to be approximately 10% of the original detailed simulations using

TABLE IV
Total Elapsed Time and Number of Floating Point Operations Required for the Full and Reduced Model Simulations

Computational procedure	RF cycles	Elapsed time (s), floating-pt ops	Time, Fl-pt ops/cycle
Full model ($N = 100$)	2000	6.05e+04, 4.12e+12	30.26, 2.06e+09
Full model	1000	4.33e+04, 3.06e+12	43.26, 3.06e+09
Full model	250	1.28e+04, 9.05e+11	51.10, 3.62e+09
LC fixed-point, full model	5	436.52, 2.98e+10	87.30, 5.95e+09
Generation of reduced basis	—	1.8, 1.39e+07	—
Reduced model ($N_1 = 22, N_2 = 8$)	2000	6.44e+03, 4.72e + 11	3.22, 2.36e + 08
Reduced model	1000	3.50e+03, 2.51e+11	3.50, 2.51e+08
Reduced model	250	1.03e+03, 7.61e+10	4.13, 3.04e+08
LC fixed-point, reduced model	5	33.30, 2.31e+09	6.66, 4.62e+08

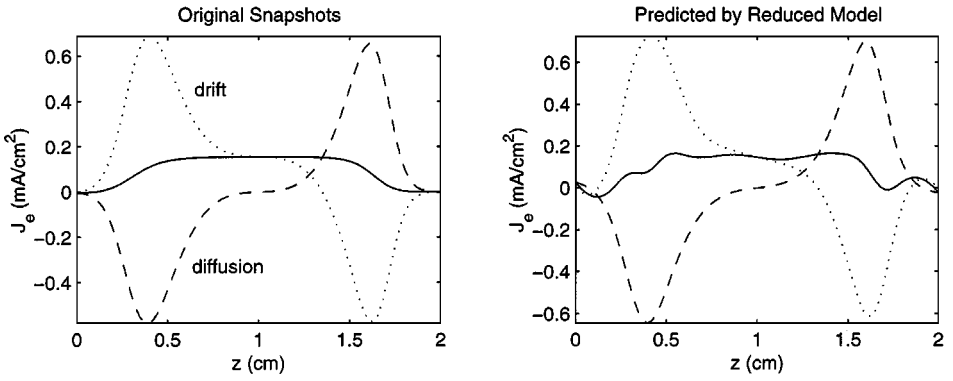*Note.* Each RF cycle consists of four time intervals (see Fig. 3).

FIG. 7. Limitations of the reduced model for $N_1 = 8$, $N_2 = 3$, demonstrated by the poor prediction of the electron flux profile J_e during the 60th cycle.

the Chebyshev collocation method, illustrating the computational benefits of the model reduction procedure.

4.2.4. Reduced-model simulator limitations. It was shown in the previous section that some of the derived quantities such as ion current are accurately captured by the reduced-basis model predictions. However, accuracy of reduced-model predictions of electron current erodes quickly from the relatively accurate predictions shown in Fig. 6 when the truncation numbers N_1 and N_2 are reduced from the values used to produce these results. For example, Fig. 7 shows a comparison between reduced and full-order simulator predictions of predicted electron current for such a case. The smooth original electron total current (solid curve) is due to the smooth diffusion and drift flux profiles. However, in the prediction produced by the reduced model, the (apparently smooth) diffusion and drift currents do not produce a smooth electron current unless the number of eigenmodes for the first set of equations is increased to at least 12. This suggests that the electron current predictions are sensitive to the tail of the eigenmodes and that the higher order modes play an important role in obtaining converged solutions when using the reduced-basis Galerkin projection method for this application. Therefore, we conclude that the number of eigenmodes needed in practical applications of model reduction methods does not depend solely on the analysis of the normalized partial sum of POD mode eigenvalues (Table III).

5. CONCLUSIONS

The physics of an argon plasma under 1 torr and 40 volts RF forcing was simulated using a Chebyshev collocation method, and the data were used to produce a reduced-order model. The detailed simulation results correctly reflected the physics of the argon plasma under consideration. Numerical residual analysis techniques were developed and used to examine solution convergence as a function of trial function truncation number. Model reduction results of the RF plasma simulation were also reported. In developing this procedure, it was found that the set of empirically determined eigenfunctions should be separated into two groups according to their type of boundary conditions. With this approach, it was found that the state variables can be accurately predicted using the empirical eigenfunctions. However,

it was also found that the prediction of the electron current by the reduced model may not be necessarily accurate.

Although accurate prediction of electron current is not a major concern in plasma processing applications, the prediction accuracy of this quantity potentially can be improved via two methods. The first approach is to use the nonlinear Galerkin method [1–4]. Higher order trial function expansions can be used for simulations in this framework by slaving the added modes to the primary dynamic modes. In other words, the long term dynamic behavior of the system is dictated by the relatively slow modes while the slaved fast modes are assumed to be at steady state with respect to the current state of the slow modes. A second method for improving the accuracy of predicted secondary quantities is to use the partial least-squares projection (PLS) to generate an additional set of empirical eigenfunctions. The PLS method can be used to define a reduced basis for the secondary quantities and to determine the linear relationship between the state variables accurately predicted by the reduced model and the corresponding secondary quantities.

REFERENCES

1. C. Foias, M. S. Jolly, I. G. Kevrekidis, G. R. Sell, and E. S. Titi, On the computation of inertial manifolds, *Phys. Lett. A.* **131**, Nos. 7 and 8, 433 (1988).

2. P. D. Christofides and P. Daoutidis, Nonlinear control of diffusion-convection-reaction processes, *Comput. Chem. Eng. Suppl.* **20**, s 1071 (1996).

3. P. D. Christofides and P. Daoutidis, Finite-dimensional control of parabolic PDE systems using approximate inertial manifolds, *J. Math. Anal. Appl.* **216**, 398 (1997).

4. H. Sano and N. Kunimatsu, An application of inertial manifold theory to boundary stabilization of semilinear diffusion systems, *J. Math. Anal. Appl.* **196**, 18 (1995).

5. P. Holmes, J. L. Lumley, and G. Berkooz, *Turbulence, Coherent Structures, Dynamical Systems and Symmetry*, Cambridge Univ. Press, Cambridge, UK, 1996.

6. L. Sirovich, B. W. Knight, and J. D. Rodriguez, Optimal low-dimensional dynamical approximations, *Quart. Appl. Math.* **XLVIII**, No. 3, 535 (1990).

7. A. Theodoropoulou, R. A. Adomaitis, and E. Zafiriou, Model reduction for optimization of rapid thermal chemical vapor deposition systems, *IEEE Trans. Semicond. Manuf.* **11**, No. 1, 85 (1998).

8. A. E. Deane, I. G. Kevrekidis, G. E. Karniadakis, and S. A. Orszag, Low-dimensional models for complex geometry flows: Application to grooved channels and circular cylinders, *Phys. Fluids A* **3**, No. 10, 2337 (1991).

9. S. Banerjee, J. V. Cole, and K. F. Jensen, Nonlinear model reduction strategies for rapid thermal processing systems, *IEEE Trans. Semicond. Manufact.* **11**, No. 2, 266 (1998).

10. H. Aling, S. Banerjee, A. K. Bangia, V. Cole, J. Ebert, A. Emami-Naeini, K. F. Jensen, I. G. Kevrekidis, and S. Shvartsman, Nonlinear model reduction for simulation and control of rapid thermal processing, in *Proceeding of the American Control Conference* (1997), p. 2233.

11. S. Y. Shvartsman and I. G. Kevrekidis, Nonlinear model reduction for control of distributed systems: A computer-assisted study, *AIChE J.* **44**, No. 7, 1579 (1998).

12. H. M. Park and D. H. Cho, Low dimensional modeling of flow reactors, *Int. J. Heat Mass Transfer* **39**, No. 16, 3311 (1996).

13. H. M. Park, T. H. Kim, and D. H. Cho, Estimation of parameters in flow reactors using the Karhunen–Loéve decomposition, *Comput. Chem. Eng.* **23**, 109 (1998).

14. H. M. Park and M. W. Lee, An efficient method of solving the Navier–Stokes equations for flow control, *Int. J. Numer. Methods Eng.* **41**, 1133 (1998).

15. D. B. Graves and K. F. Jensen, A continuum model of DC and RF discharges, *IEEE Trans. Plasma Sci.* **14**, No. 2, 78 (1986).

16. M. Meyyappan, Ed. *Computational Modeling in Semiconductor Processing* (Artech House, Boston, 1995).

17. Y.-H. Lin and R. A. Adomaitis, A global basis function approach to DC glow discharge simulation, *Phys. Lett. A* **243**, No. 3, 142 (1998). [Also in ISR TR 97-81]

18. L. E. Kline and M. J. Kushner, Computer simulation of materials processing plasma discharges, *Critical Rev. Solid State Materials Sci.* **16**, No. 1, 1 (1989).

19. R. A. Adomaitis, Y.-H. Lin, and H.-Y. Chang, A computational framework for boundary-value problem based simulations, *Simulation* **74**, No. 1, 28 (2000).

20. J. D. P. Passchier and W. J. Goedheer, A two-dimensional fluid model for an argon RF discharge, *J. Appl. Phys.* **74**, No. 6, 3744 (1993).

21. J. D. P. Passchier and W. J. Goedheer, Relaxation phenomena after laser-induced photodetachment in electronegative RF discharge, *J. Appl. Phys.* **73**, No. 3, 1073 (1993).

22. A. D. Richards, B. E. Thompson, and H. H. Sawin, Continuum modeling of argon radio frequency glow discharges, *Appl. Phys. Lett.* **50**, No. 9, 492 (1987).

23. E. Gogolides and H. H. Sawin, Continuum modeling of radio frequency glow discharges. II. Parametric studies and sensitivity analysis, *J. Appl. Phys.* **72**, No. 9, 3988 (1992).

24. E. Gogolides and H. H. Sawin, Continuum modeling of radio frequency glow discharges. I. Theory and results for electropositive and electronegative gases, *J. Appl. Phys.* **72**, No. 9, 3971 (1992).

25. E. Gogolides, H. H. Sawin, and R. A. Brown, Direct calculation of time-periodic steady-state of continuum models of radio-frequency plasmas, *Chem. Eng. Sci.* **47**, Nos. 15/16, 3839 (1992).

26. G. L. Huppert, H. H. Sawin, and R. A. Brown, Spectral element analysis of radio-frequency glow discharges, *Chem. Eng. Sci.* **49**, No. 10, 1601 (1994).

27. M. J. Kushner, Advances in plasma equipment modeling, *Solid State Technol.* 135 (1996).

28. D. P. Lymberopoulos and D. J. Economou, Two-dimensional self-consistent radio frequency plasma simulations relevant to the gaseous electronics conference RF reference cell, *J. Res. Nat. Inst. Stand. Technol.* **100**, No. 4, 473 (1995).

29. M. S. Barnes, T. J. Cotler, and M. E. Elta, A stagger-mesh finite-difference numerical method for solving the transport equations in low pressure RF glow discharges, *J. Comput. Phys.* **7**, 53 (1988).

30. C. Li and C.-H. Wu, Three fluid transport models by particle-in-cell method for RF glow discharges, *IEEE Trans. Plasma Sci.* **20**, No. 6, 1000 (1992).

31. M. Surendra and D. B. Graves, Particle simulation of radio-frequency glow discharges, *IEEE Trans. Plasma Sci.* **19**, No. 2, 144 (1991).

32. A. Bogaerts and R. Gijbels, Hybrid Monte Carlo-fluid model of a direct current glow discharge, *J. Appl. Phys.* **78**, No. 4, 2233 (1995).

33. M. J. Kushner, Consequences of asymmetric pumping in low pressure plasma processing reactor: A three-dimensional modeling study, *J. Appl. Phys.* **82**, No. 11, 5312 (1997).

34. M. Meyyappan and J. P. Kreskovsky, Glow discharge simulation through solutions to the moments of the Boltzmann transport equation, *J. Appl. Phys.* **68**, No. 4, 1506 (1990).

35. B. Fornberg, *A Practical Guide to Pseudospectral Methods* (Cambridge Univ. Press, New York, 1996).

36. G. Gottlieb and S. A. Orszag, *Numerical Analysis of Spectral Methods: Theory and Applications* (Society for Industrial and Applied Mathematics, Philadelphia, 1977).

37. R. G. Rice and D. D. Do, *Applied Mathematics and Modeling for Chemical Engineers* (Wiley, New York, 1995).

38. W. H. Press, B. P. Flannery, S. A. Teukolsky, and W. T. Vetterling, *Numerical Recipes in FORTRAN: The Art of Scientific Computing*, 2nd ed. (Cambridge Press, New York, 1992).

39. Y.-H. Lin, H.-Y. Chang, and R. A. Adomaitis, MWRTOOLS: A library for weighted residual method calculations, *Comput. Chem. Eng.* **23**, 1041 (1999). [Also ISR TR 98-24]

40. L. Sirovich, Turbulence and the dynamics of coherent structures. Part I: Coherent structures, *Quart. Appl. Math.* **XLV**, No. 3, 561 (1987).

41. Y.-H. Lin, *From Detailed Simulation to Model Reduction: Development of Numerical Tools for a Plasma Processing Application*, Ph.D. thesis (The University of Maryland, College Park, 1999).